A. Ozgurluk, K. A. Peleaux, C. T.-C. Nguyen, "Single-digit-nm capacitive-gap transduced micromechanical disk resonators," *Tech. Digest*, 2020 IEEE Int. Micro Electromechanical Systems Conference, Vancouver, Canada, Jan. 18-22, 2020, pp. 222-225.

SINGLE-DIGIT-NANOMETER CAPACITIVE-GAP TRANSDUCED MICROMECHANICAL DISK RESONATORS

Alper Ozgurluk, Kieran Peleaux, and Clark T.-C. Nguyen
Department of EECS, University of California at Berkeley, Berkeley, California, USA

ABSTRACT

Single-digit-nanometer electrode-to-resonator gaps have enabled 200-MHz radial-contour mode polysilicon disk resonators with motional resistance R_x as low as 144Ω while still posting Q's exceeding 10,000, all with only 2.5V dc-bias. The demonstrated gap spacings down to 7.98nm are the smallest to date for upper-VHF micromechanical resonators and fully capitalize on the fourth power dependence of motional resistance on gap spacing. High device yield and ease of measurement debunk popular prognosticated pitfalls often associated with tiny gaps, e.g., tunneling, Casimir forces, low yield, none of which appear. The devices, however, are more susceptible to environmental contamination when unpackaged. The tiny motional resistance, together with (C_x/C_o)'s up to 1% at 4.7V dc-bias and (C_x/C_o)-Q products exceeding 100, propel polysilicon capacitive-gap transduced resonator technology to the forefront of MEMS resonator applications that put a premium on noise performance, such as radar oscillators.

KEYWORDS

Resonator, transducer, quality factor, Casimir, atomic layer deposition, motional resistance, very high frequency.

INTRODUCTION

The promise of sub-10-nm gaps has long enticed researchers pursuing capacitive-gap transduced micromechanical resonators operating at upper-VHF and beyond. This is because the theoretical fourth order dependence of motional resistance on electrode-to-resonator gap spacing predicts that capacitive-gap transduced resonators will outperform piezoelectric ones in both coupling and Q when gaps get below a certain threshold. Indeed, the former already outperform the latter in both metrics at HF and low-VHF frequencies [1], [2], [3], which is why capacitive-gap transduced resonators have dominated the MEMS timing market. At higher frequencies, e.g., upper-VHF and beyond, while capacitive-gap devices have the higher Q's, piezoelectric ones had considerably higher coupling. That is, until now. The 7.98nm gaps demonstrated herein offer 7.5 times motional resistance R_x reduction over [2] and for the first time enable capacitive-gap transduced resonators at 200 MHz with R_x of 144Ω and a (C_x/C_o)-Q ~100, more than 2 times that of the nearest previously published upper-VHF (i.e., 150-300 MHz) resonators [4], [5].

This paper briefly details the theory, fabrication, and demonstration of single-digit-nm gap polysilicon resonators, then illustrates how the equivalent circuits of such devices enable oscillator and filtering applications that could catapult MEMS-based timing and frequency control capabilities to levels that permit greater cognitive abilities in communication systems [6].

DEVICE OPERATION AND MODEL

Fig. 1 presents a perspective view of the disk resonator

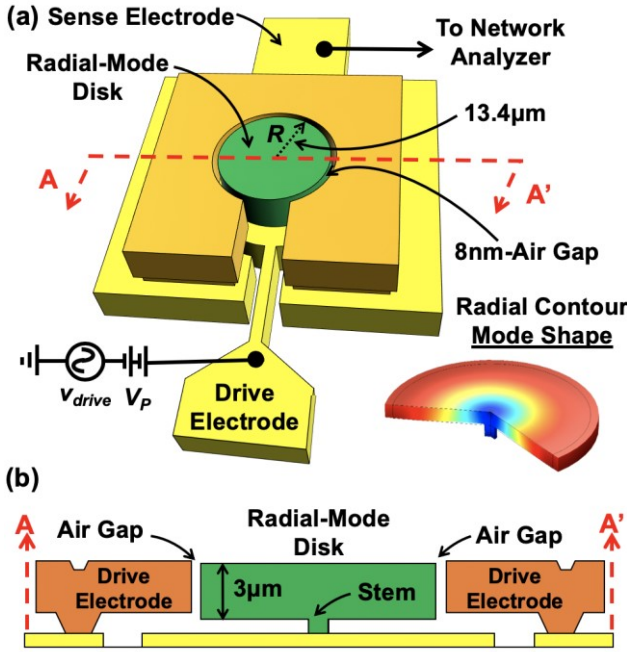

Fig. 1: (a) The contour mode disk resonator described herein in a typical operating circuit with dimensions and the mode shape. (b) Device cross-section.

in a typical bias and excitation circuit, together with dimensions and operating mode shape. The device is similar in structure to that of [2] but differs in its much smaller gap spacing and in its use of 3-μm-thick interconnects to reduce interconnect resistance, which helps to isolate the intrinsic Q and motional resistance during measurement.

The device operates by vibrating upon application of an appropriate combination of dc-bias V_P plus ac excitation v_{drive} across its electrode-to-resonator gap [7], where excitation at its radial-contour mode resonance frequency induces vibration in the mode shape depicted in Fig. 1(a). The resulting dc-biased time-varying electrode-to-resonator capacitance then sources an output current across the device terminals in Fig. 1(a). The magnitude of current at resonance is governed by the motional resistance R_x in the condensed equivalent circuit of Fig. 2, which takes the form

$$R_x = \frac{\chi K_{mat}\sqrt{E\rho}\,d_o^4}{16QV_p^2\varepsilon_o^2RH} \qquad (1)$$

where Q is the quality factor, V_P is the dc-bias, d_o is the air gap, ε_o is the vacuum permittivity, R is the disk radius, H is the disk thickness, χ is a constant that relates the static mass of the disk to its dynamic mass [7], K_{mat} is a dimensionless frequency parameter [7], E is the Young's modulus of the resonator structural material, and ρ is the density of the resonator structural material. Here, the smaller the R_x, the larger the current, so many applications prefer a small R_x. This, together with the fourth power dependence of R_x on electrode-to-resonator gap spacing d_o, fuels the

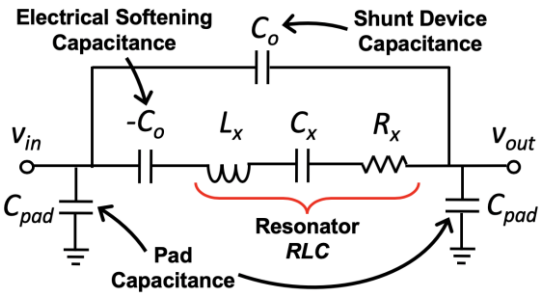

Fig. 2: Condensed equivalent circuit between the drive and sense terminals of the Fig. 1 device.

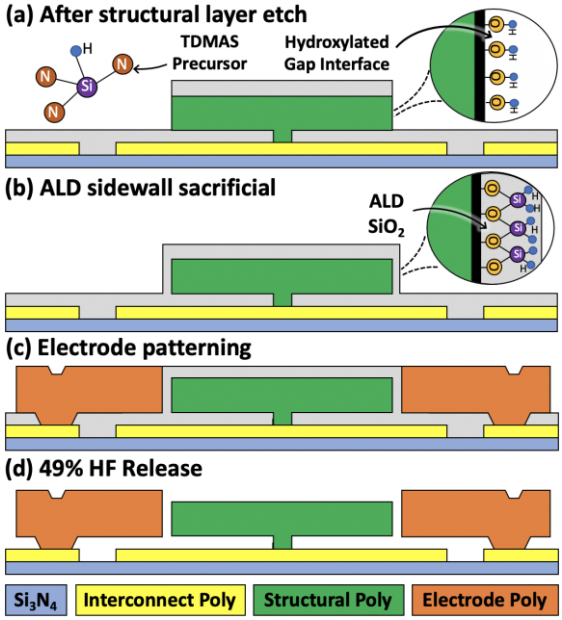

Fig. 3: Portions of the fabrication process flow focusing on the ALD sidewall sacrificial spacer that defines the single-digit-nm gap.

desire to shrink d_o.

The device becomes more effective in various applications as the ratio of C_x to C_o in the Fig. 2 equivalent circuit rises. In designable parameters, this ratio takes the form

$$\frac{C_x}{C_o} = \frac{V_P^2}{d_o^3}\frac{\varepsilon_o R \theta_{ov}}{\pi^3 \chi K_{mat}^2 E} \qquad (2)$$

where again shrinking d_o very quickly improves the metric. Next generation timing and RF channel-select applications expected to enable transformative changes [6] [8] prefer simultaneous Q and C_x/C_o in the range of >10,000 and ~1%, respectively.

FABRICATION

Fig. 3 briefly summarizes the surface-micromachining fabrication process that achieves single-digit-nm-gap devices, largely based on the process used in [9]. The main difference from [9] is the critical gap-defining step of Fig. 3(b), which now employs an ultra-smooth polysilicon etch recipe [2], careful cleaning, and ample hydroxylation before an SiO_2 ALD step that establishes the sub-10-nm gap defining oxide. The use of ALD in lieu of the LPCVD high temperature oxide deposition of previous processes [2] outright enables the tiny gaps achieved here.

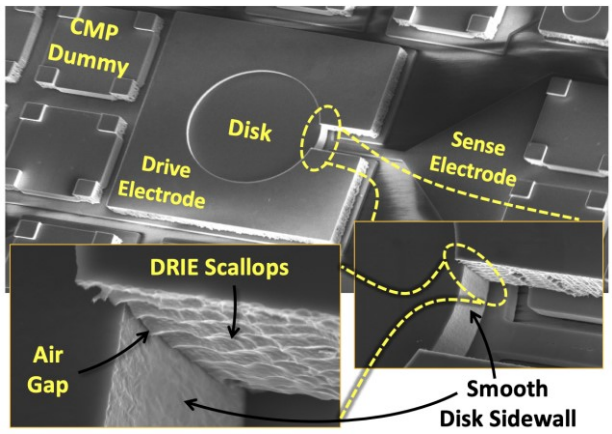

Fig. 4: SEM of a fabricated single-digit-nm gap contour mode polysilicon disk resonator.

The next most critical step in the process is the device release, which now entails multiple piranha and HF soaks to adequately clear the gaps. Contrary to popular expectation, residual stress was not a big concern, as the process permits a surprisingly high (>90%) functional device yield, even without a stress anneal. Fig. 4 presents wide-view and zoom-in SEMs of a fabricated 8-nm-gap disk resonator, emphasizing the much smoother resonator sidewalls than electrode sidewalls, the latter of which were etched via a conventional DRIE recipe.

RESULTS AND DISCUSSION

For comparative purposes, the fabrication process achieved not only single-digit-nm gaps via ALD, but also larger gaps from 10 nm to 80 nm via appropriate deposition types, e.g., LPCVD. Once released, devices were quickly transferred into a Lakeshore FWPX Vacuum Probe Station that provided a 100 μTorr vacuum environment as well as probes and access ports that connect to outside measurement instrumentation. In actual measurement, an Agilent E5071C network analyzer provided the drive signal and sense port in the circuit of Fig. 1(a).

For single-digit-nm gap devices, the best experimental results came upon immediate measurement after release—something not needed for larger gap devices. Longer wait times between release and measurement resulted in degraded performance, e.g., lower Q, suggesting larger susceptibility to contamination, e.g., moisture condensation, which one might expect with gaps this small. Once in vacuum, however, devices stabilized and other popular concerns about gaps this small, whether real or mythical, e.g., tunneling, Casimir forces, did not materialize.

Fig. 5(a) presents vacuum-measured transmission spectra (both actual and sans parasitic interconnect/measurement resistance) versus dc-bias for a 13.4μm-radius radial-contour mode polysilicon disk, showing a 199.8 to 199.5-MHz frequency excursion over 0.6 to 2.5V with a Q of 12,298 at 0.6V. Fig. 5(b) presents a curve fit of resonance frequency versus dc-bias using electrical stiffness theory [7] that confirms an electrode-to-resonator gap spacing of 7.98nm. The scale here is perhaps best conveyed with the recognition that this gap corresponds to only 20-25 SiO_2 molecules!

While Casimir effects were not seen, theory predicts

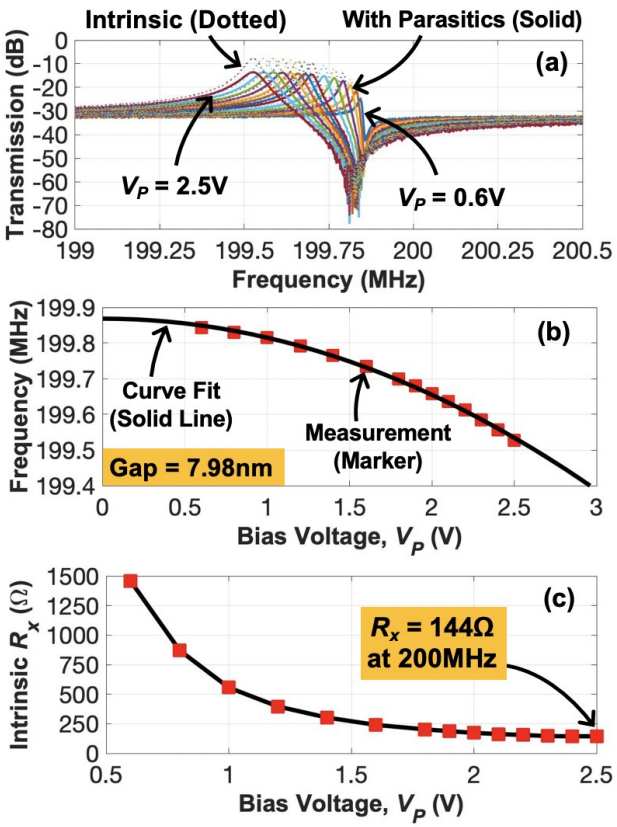

Fig. 5: (a) Measured frequency spectra as a function of dc-bias voltage that permit (b) curve-fitted extraction of the gap value and (c) a plot of motional resistance vs. V_P.

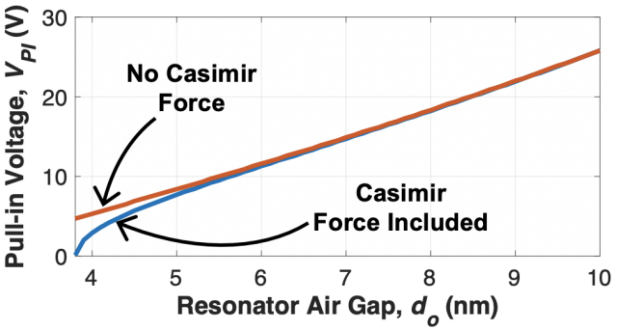

Fig. 6: Plot of pull-in voltage including and not including Casimir force, confirming our inability to see their influence even in the 8-nm-gap device.

that their influence is imminent as gaps continue to shrink. For instance, when accounting for Casimir force, the expressions governing the dc-bias voltage that pulls (or stretches) the disk into its electrode take the form

$$\frac{3d_{PI}}{2} - d_o = \frac{\pi^2 \hbar c R \theta_{ov}}{240 d_{PI}^4 k_r}$$
$$V_{PI}^2 = \frac{k_r d_{PI}^3}{\varepsilon_o A_{ov}} - \frac{\pi^2 \hbar c}{60 \varepsilon_o d_{PI}^2} \quad (3)$$

where V_{PI} is the pull-in voltage, d_{PI} is the critical pull-in gap spacing, $\hbar$ is the modified Planck's constant, c is the speed of light, and k_r is the effective resonator stiffness. Fig. 6 solves and plots (3) against the traditional expression for pull-in voltage [10], suggesting that Casimir forces begin to influence when the gap approaches 6 nm, so are not yet apparent for the current 8-nm gap device. Using (3),

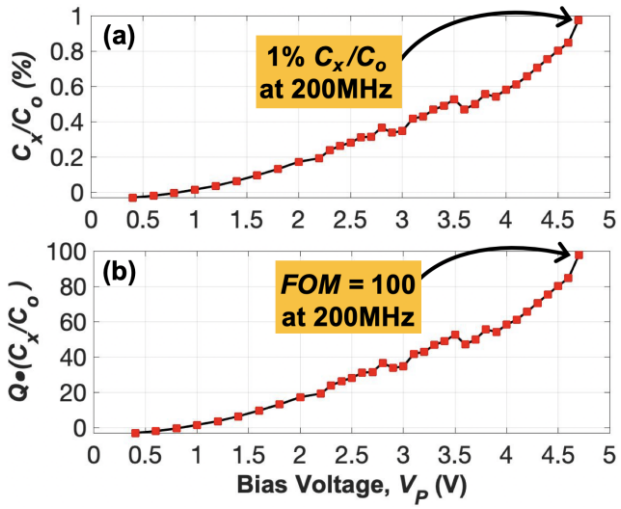

Fig. 7: Measured (C_x/C_o) and (C_x/C_o)-Q as functions of dc-bias voltage for a 9.4-nm-gap 200-MHz disk.

the predicted pull-in voltage for the 8-nm-gap disk of Fig. 1 of 18.3V still permits a calculated motional resistance of 0.2Ω, which is quite small.

Unfortunately, devices pulled in well before 18.3V, possibly because (3) assumes the disk stretches symmetrically into the electrode and ignores the possibility of stem failure. Although dc-bias constraints precluded R_x's as low as 0.2Ω, they still permitted unprecedented low values for capacitive-gap transduced disks. For example, Fig. 7 shows a plot of measured motional resistance R_x versus dc-bias for a 9.4-nm-gap 200-MHz device, where 2.5V yields only 144Ω, which is commensurate with conventional RF applications. Fig.7 presents the corresponding plot of (C_x/C_o)-Q, showing an impressive figure of merit of 100.

Fig. 8 compares the performance of 200-MHz polysilicon disk resonators with varying electrode-to-resonator gaps. Here, even though smaller gaps impose smaller maximum dc-bias voltages and seem to slightly reduce Q, they still enable higher (C_x/C_o)'s, as well as (C_x/C_o)-Q's, both of which increase as $1/d_o^{1.30}$. The figure also shows how R_x still decreases as $d_o^{1.52}$ when accounting for the observed dc-bias and Q constraints.

Table 1 compares the device of Fig. 1 with other upper-VHF MEMS resonators in the literature using various transducers, showing clear advantages.

APPLICATION OPPORTUNITIES

The expected impact of 8-nm electrode-to-resonator gaps perhaps best manifests in the applications they make possible. For instance, the simultaneous coupling of 1% with Q of 12,298 makes possible a Fig. 2 equivalent circuit with L_x = 223.55μH, C_x = 2.83fF, R_x = 22.84Ω, and C_o = 283fF that in turn enables channel-select filters using many more resonators than demonstrated in [9].

To illustrate, Fig. 8 presents frequency response simulations for Chebyshev filters like that of [9] but centered at 200 MHz with bandwidths of 400 kHz and using three resonators instead of just two for sharper passband to stopband transitions. One simulation (dotted line) assumes resonators like those of [9], with 40-nm gaps, with consequent passband distortion that renders the response problematic

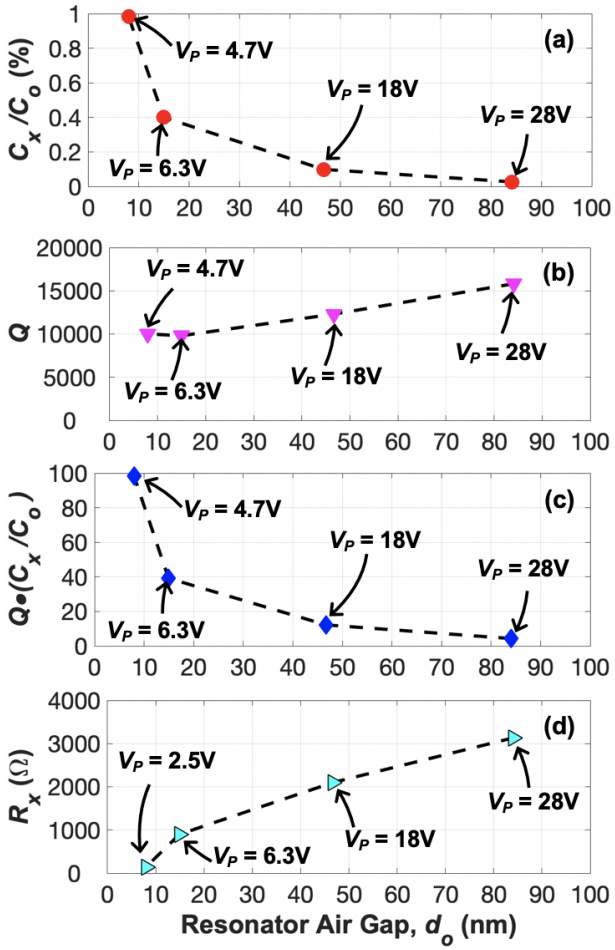

Fig. 8: Plots of various measured parameters versus electrode-to-resonator gap showing marked improvement in

for RF channel-selection. A second simulation (dashed-dotted line) assumes resonators with Q and (C_x/C_o) achieved by AlN near 200 MHz [4], but results in even worse performance than the capacitive-gap transduced resonators of [9].

The solid curve finally corresponds to a filter simulation assuming resonators demonstrated herein with 8-nm gaps, for which passband distortion is no longer discernable. The solid curve is the only one usable for software-defined cognitive radio architecture scheme of [6].

CONCLUSIONS

The demonstration herein of capacitive-gap transduced resonators with single-digit-nm electrode-to-resonator gaps now makes possible (C_x/C_o)-Q's up to 100 at upper-VHF frequencies that in turn enable simultaneous high Q >10,000 and low motional resistance <150Ω using sub-3V bias voltages. That capacitive-gap transduced resonators achieve this is especially significant for applications that require exceptional long-term stability, for which single-material resonators have historically performed best. The low-loss, stability, and strong coupling achieved here now propels capacitive-gap transduced devices towards high performance oscillator applications, e.g., low phase noise radar oscillators, and encourages research on transformative communication paradigms, such as RF channel-select-enabled software-defined cognitive radio. While 200-MHz is already useful for each of these applications, higher frequency is always welcome. Gigahertz resonators with single-digit-nm gaps are likely on the horizon.

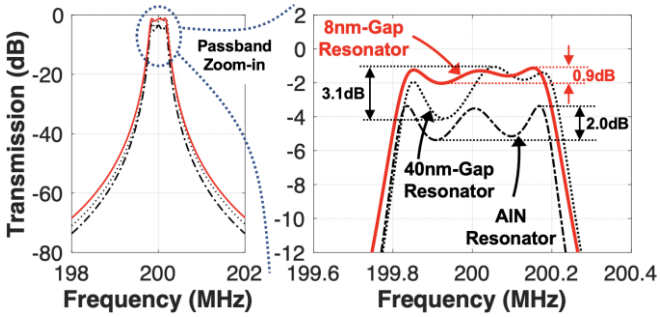

Fig. 9: Frequency response simulations for an RF channel-select Chebyshev bandpass filter using previous resonators versus the new 8-nm-gap resonators.

Table 1: Comparison chart with other technologies.

Ref.	f_o (MHz)	C_x/C_o (%)	R_x (Ω)	Q	k_t^2-Q	*Area* (μm²)
[11][a]	85	0.86	125	2,100	18	10,000
[5][b]	108	0.70	-	6,300	50	72,000
[4][a]	220	1.60	-	2,500	40	9,000
[12][c]	149	0.48	460	10,000	48	21,200
[2][d]	60	1.62	54	29,640	480	3,200
[13][d]	123	0.75	1,250	2,271	17	1,600
This Work[d]	200	1.00	144	12,298	100	718

[a]Piezoelectric, [b]Piezoelectric-on-Si, [c]Quartz, [d]Capacitive

REFERENCES

[1] A. Ozgurluk et al., "Q-boosting of metal MEMS resonators via localized anneal…," DOI: 10.1109/FCS.2017.8088786.

[2] J. N. Nilchi et al., " High Cx/Co 13nm-capacitive-gap transduced…," DOI:10.1109/MEMSYS.2017.7863560.

[3] A. Ozgurluk et al., "Widely tunable 20-nm-gap ruthenium metal square…," DOI: 10.1109/MEMSYS.2019.8870623.

[4] S. I. Jung et al., " The Impact of Bottom Electrode Cove…," DOI: 10.1109/TRANSDUCERS.2019.8808532.

[5] M. Ghatge et al., "High k2t·Q waveguide-based ScAlN-on-Si UHF and…," DOI: 10.1109/FCS.2018.8597447.

[6] C. T.-C. Nguyen, "MEMS-based RF channel selection for true software…," DOI: 10.1109/MCOM.2013.6495769.

[7] M. Akgul et al., "A negative-capacitance equivalent circuit model for parallel-pl…," DOI:10.1109/TUFFC.2014.2976.

[8] A. Ozgurluk et al., "RF channel-select micromechanical disk filters-Part I…," DOI: 10.1109/TUFFC.2018.2881727

[9] M. Akgul et al., "RF channel-select micromechanical disk filters-Part II…," DOI: 10.1109/TUFFC.2018.2883296.

[10] H. C. Nathanson et al., "The resonant gate transistor," DOI: 10.1109/T-ED.1967.15912.

[11] G. Piazza et al., "Piezoelectric aluminum nitrode vibrating contour-mode…," DOI: 10.1109/JMEMS.2006.886012.

[12] F. P. Stratton et al., "A MEMS-based quartz resonator technology for…," DOI: 10.1109/FREQ.2004.1418425.

[13] A. Ozgurluk et al., "High-Cx/Co hollow disk resonators," DOI: 10.1109/FCS.2018.8597505.